



Finite element modeling and experiment for behavior estimation of AlMn0.5Mg0.5 sheet during electromagnetic forming

Dorin LUCA

Department of Technologies and Equipments for Materials Processing,
Technical University of Iasi, Iasi 700050, Romania

Received 9 September 2014; accepted 27 March 2015

Abstract: The electromagnetic forming is a procedure of high-speed processing, which favors the increase of the formability of some plastically deformed metals. In order to evaluate the capacity of some light metals, such as aluminum and its alloys, to be deformed through this procedure, it is useful to know the stress and strain state that occurs in the material during forming. In this work, the modeling of stresses and strains in electromagnetically deformed AlMn0.5Mg0.5 sheet was made. The modeling was achieved using the finite element method and it was verified through experimental tests. To determine the residual stresses, the X-ray diffraction method was used. The strains were established by measuring the displacements of the nodes in the network inscribed on the specimen by means of three coordinates measuring machine. A good agreement between the modeling results and experimental data was found.

Key words: finite element modeling; electromagnetic forming; AlMn0.5Mg0.5 sheet; X-ray diffraction; stress; strain

1 Introduction

In the last few years, researches regarding electromagnetic forming (EMF) of metal sheets have been accentuated, as a result of the demands of automotive industry to manufacture lighter vehicles in order to reduce the fuel consumption and pollution [1]. A solution to manufacture these vehicles is the use of lightweight materials such as aluminum and its alloys, for replacing the steel in the car body structure, being possible to reduce its mass by about 50% [2].

The increasing interest for applying EMF in manufacturing of light body elements for vehicles is strongly related to the procedure's capacity to increase the forming limits of metals such as aluminum or other metals with limited formability [3,4].

Since 1999, VOHNOUT et al [5] has conducted an experimental research in order to apply the EMF to auto parts. There was an attempted execution of 6011-T4 aluminum doors inners, of steel as well, demonstrating the ability of EMF to reduce or even suppress wrinkling material [6,7] and to increase the formability of the material [8,9]. To explain the change of the material formability, it is important to know the distribution of

strains and stresses.

In 2003, only 2%–3% of passenger cars used intensive aluminum because of greater cost compared to steel, disadvantages related to low formability and large spring back occurring as well [10]. Studies were conducted in collaboration with PSA Peugeot Citroen on aluminum 1050 sheet electromagnetically deformed.

In 2005, there are reports concerning the application of EMF to perform some joints in the automotive body as well [11]. Among lightweight materials, such as aluminum and its alloys, magnesium and its alloys or plastics, the use of high-strength aluminum alloy in the automotive industry is increasing every year [12].

Numerical modeling of the behavior during EMF of some aluminum alloys was approached by several researchers. One of the first numerical modeling of EMF process can be attributed to TAKATSU et al [13], who analyzed the way of free bulging of a clamped disk from aluminum. Some researchers performed modeling by finite difference method. FENTON and DAEHN [2] achieved a modeling of Takatsu experiment using finite difference method and found similar results. CORREIA et al [14] used a subroutine of the code ABAQUS/Explicit to enter a finite differences code with which electromagnetic parameters that produce a magnetic

pressure as high as possible were calculated. It should be noted that the results set out in the finite difference modeling everything were compared to the experimental results provided by TAKATSU et al [13].

The most common method of modeling the EMF processes remains to be the finite element method, being signaled its applications both at the modeling plastic deformation of metal sheets and tubes.

AHMED et al [15] modeled the magnetic force distribution and magnetic field at flat spiral coils using finite element software ANSYS. Recently, CUI et al [16] used the finite element software ANSYS/LS-DYNA for modeling the distribution of the magnetic force on a new type of flat electromagnetic actuator that produces a uniformly distributed pressure deformation.

The problem of electromagnetic bulging tube modeling has been approached in a large number of researches. LI et al [17] investigated by numerical simulations with finite element of the electromagnetic bulging tube using ANSYS software. At the same time, KARCH and ROLL [18] raised the question of considering the thermal effects that occur in the EMF system due to the heating by eddy currents (Joule effect), and mechanical work of plastic deformation. They obtained transient simulations of EMF process occurring in aluminum tubes. The proposed model made predictions on the electromagnetic field, temperature, pressure and stress during the deformation process.

CAO et al [19] presented a precise method for analyzing the dynamic behavior of the workpiece in electromagnetic forming process, developed using COMSOL multiphysics software. The method performed full coupling between electromagnetic fields and plastic deformation of the workpiece, by considering the effects of the sheet geometry and velocity on the discharge current, magnetic forces and plastic deformation of the workpiece.

The 2D modeling and simulation of EMF processes which present plane or axial symmetry were mostly treated [2, 10, 13–15, 17–19, 20–26] and lesser on 3D [16, 27–29].

In this work, 2D finite element modeling of an EMF process applied to metal sheet from AlMn0.5Mg0.5 aluminum alloy was achieved. Studies on the behavior of this material during deformation with high speeds do not appear in the scientific papers in the field.

2 Material testing for correctly modeling of process

AlMn0.5Mg0.5 (EN AW-3105 series) has good resistance to corrosion, good anodizing ability, good formability, good weldability and good brazeability [30].

These properties show that this material may be used to manufacture sheet metal parts for cars.

The chosen material for experimental tests was subjected to tensile tests with the aim of determining its elastic, plastic and viscous properties. Tests were performed at room temperature (20 °C), with the requirements of ISO 6892-1:2009. The specimens for tensile tests were cut off so that the load axis formed angles of 0°, 45° and 90° with the sheet rolling direction. The registered tensile curves are illustrated in Fig. 1. Tensile tests were performed on an automatic MTS 810.24 testing machine (Material Test System) with precision class 1, hydraulically actuated and equipped with an automatic data acquisition system.

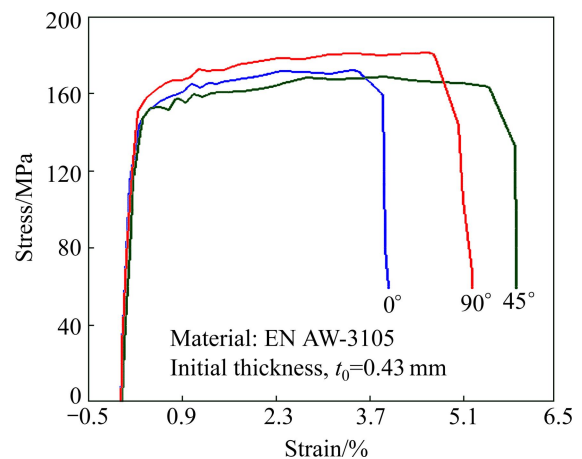


Fig. 1 Obtained tensile curves of tested material

The results provided for elastic and plastic characteristics of the tested material are shown in Table 1 where E is the elastic modulus, $R_{p0.2}$ is the yield strength, R_m is the ultimate tensile strength and A_{80} is the elongation at fracture on 80 mm.

Table 1 Characteristic values of tested material determined by tensile tests

Angle to rolling direction/(°)	E /GPa	$R_{p0.2}$ /MPa	R_m /MPa	A_{80} /%
0	78.764	158.136	173.714	3.050
45	78.518	152.550	169.436	4.953
90	82.198	165.656	182.066	3.845
Average value	79.827	158.781	175.072	3.949

Strain hardening exponent n was determined, according to the current standards, for all homogeneous plastic deformation range from mathematical equation that expresses true stress–true strain and can be depicted as

$$\sigma = K \cdot \varepsilon^n \quad (1)$$

where σ is the applied stress on the material, K is the strength coefficient, and ε is the strain.

After transforming Eq. (1) into a logarithmic equation and then its linearization, the strain hardening exponent n was calculated, using the least squares method with equation:

$$n = \frac{N \sum_{i=1}^N x_i y_i - \sum_{i=1}^N x_i \sum_{i=1}^N y_i}{N \sum_{i=1}^N x_i^2 - \left(\sum_{i=1}^N x_i \right)^2} \quad (2)$$

where N is the number of points established for calculation (20 points), $y = \ln \sigma$, $x = \ln \dot{\epsilon}$.

Applying the above procedure, out of the performed tensile tests, the strain hardening exponent values n indicated in Table 2 were determined for the used material. The strength coefficient values K which are numerically equal with the extrapolated values of true stress for the true strain to value 1.00 were determined as well.

Table 2 Determined values of n and K coefficients

Angle to rolling direction/(°)	n	K/MPa
0	0.110	235.276
45	0.095	208.705
90	0.125	235.811
Weighted average values	0.106	222.124

Taking into account the recommendations contained in the literatures, the strain hardening exponent was considered as a weighted average of the values determined for the three types of specimens tested, calculated with the equation:

$$\bar{n} = \frac{n_0 + n_{90} + 2n_{45}}{4} \quad (3)$$

where n_0 , n_{90} , n_{45} are strain hardening exponents established for the specimens of 0°, 90°, and 45° codes according to Table 2.

The strain-rate sensitivity exponent m was determined using the relationship between true stress (σ) and true strain rate ($\dot{\epsilon}$):

$$\sigma = K \cdot \dot{\epsilon}^m \quad (4)$$

where K is the strength coefficient ($K = \sigma$ for $\dot{\epsilon} = 1$).

Applying the logarithm on Eq. (4) results in

$$\ln \sigma = \ln K + m \ln \dot{\epsilon} \quad (5)$$

The m value is the same for different strain rates because in coordinates $\ln \sigma - \ln \dot{\epsilon}$, Eq. (5) represents a straight line. In particular, the m value is valid for high-speed processes (e.g., EMF).

To determine the exponent m for EN AW-3105 aluminum alloy, tensile tests were performed with three velocities v_1 , v_2 and v_3 using the same type (non-proportional) of specimens like those used to determine exponent n . From the $\sigma - \epsilon$ curves drawn with velocities v_1 , v_2 and v_3 , the stress values σ_1 , σ_2 and σ_3 for a same strain were extracted.

Assuming that plastic deformation is homogeneous, the corresponding strain rates were calculated with relationship:

$$\dot{\epsilon} = v / L_0 \quad (6)$$

where v is the gripping wedges speed of testing machine and L_0 is the original gauge length ($L_0=45$ mm).

Using extrapolation procedure [31] for two stresses σ_1 and σ_2 corresponding to strain rates $\dot{\epsilon}_1$ and $\dot{\epsilon}_2$, the m value can be obtained as

$$m = (\ln \frac{\sigma_2}{\sigma_1}) / (\ln \frac{\dot{\epsilon}_2}{\dot{\epsilon}_1}) \quad (7)$$

Using pairs of values, the graphs of $\sigma - \dot{\epsilon}$ and $\ln \sigma - \ln \dot{\epsilon}$ was drawn (Fig. 2) and the strain-rate sensitivity exponent m was determined.

The EN AW-305 alloy analyzed in this work has the chemical composition specified in Table 3.

The material density experimentally determined is 2710.299 kg/m³.

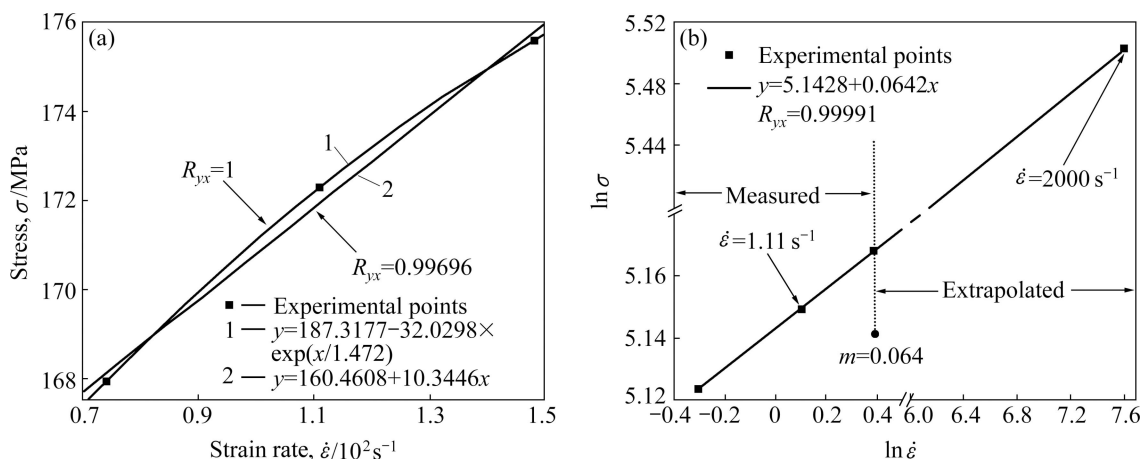


Fig. 2 Dependencies of $\sigma - \dot{\epsilon}$ (a) and $\ln \sigma - \ln \dot{\epsilon}$ (b) for EN AW-3105 alloy

Table 3 Chemical compositions of EN AW-3105 alloy (mass fraction, %) (sheet thickness 0.43 mm)

Si	Fe	Cu	Mn	Mg
0.27	0.33	0.11	0.46	0.72
Cr	Zn	Ti	Others (Ni)	Al
0.069	0.030	0.019	0.050	Balance

3 Finite elements modeling

The loading of the model consisted in specifying the deformation pressure distribution (magnetic pressure) after its determination by means of FLUX2D software. The deformation pressure was calculated considering the differences between the magnetic inductions on the opposite surfaces of the specimen, according to the equation:

$$p = \frac{1}{2\mu} (B_1^2 - B_2^2) \quad (8)$$

where μ is the magnetic permeability, B_1 is the magnetic induction on the upper surface of the specimen and B_2 is the magnetic induction on the lower surface of the specimen.

The simulated values of the discharged current through the coil and the magnetic induction were confronted by its experimental measurements (Fig. 3). Measurements of magnetic induction and of the current through the coil were performed simultaneously, using a data acquisition system consisting of transducers, digital oscilloscope with memory and laptop. The measurement of the magnetic induction at various points was performed using a coil transducer, lamella type, which was introduced through an aperture in the space between the coil and the workpiece.

Then, the variation in time of the deformation pressure components was specified (axial and radial). After determining the magnetic pressure variation (in space and time) with FLUX2D software, numerical data were exported in ALGOR software for modeling the mechanical behavior of the AlMn0.5Mg0.5 sheet.

This procedure was adopted by SIDDIQUI et al [20] for modeling electromagnetic bulging of the metal sheet, using the pair of programs FEMM–ABAQUS. The pressure pulse applied to specimen was obtained by energy discharge of 1.6 kJ, charged into the capacitor bank, corresponding to some values of the parameter commonly used in experimental research: 4 kV voltage and 200 μ F capacitance. The flat spiral coil is made of copper with high purity and it has 9 turns with the section of 1.2 mm \times 10.1 mm. The specimen of the AlMn0.5Mg0.5 aluminum alloy has 110 mm diameter and 0.43 mm thickness, and the obtained deformed part has 80 mm diameter.

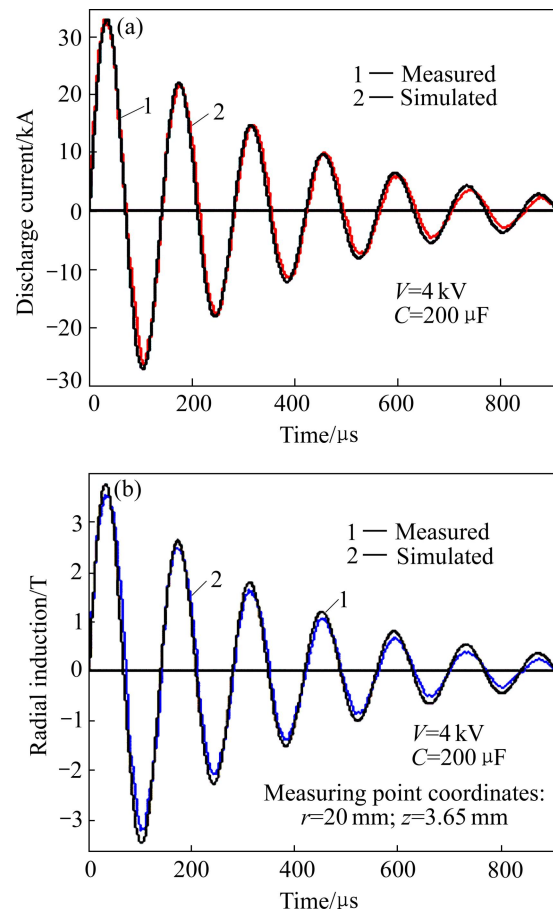


Fig. 3 Variation in time for discharge current through coil (a) and radial induction (b)

For presenting the simulation results for electromagnetic parameters, the image of vectors of magnetic pressure distribution on the surface of the disk specimen (Fig. 4), corresponding to the transient evolution of the magnetic field at the beginning of electromagnetic forming process (time, 0.1 μ s), has been chosen.

Because of the high speed of the EMF process, the material of the workpiece will have a viscoplastic behavior during the forming process in desired shape. In modeling of such a process, which is appointed to the

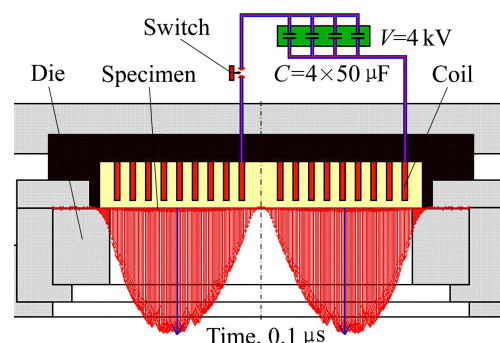


Fig. 4 Pressure deformation vectors on specimen's surface

dynamic problems of plasticity, the influence of the strain rate on the behavior of the workpiece material must be considered [32]. Through a dynamic problem of plasticity (or viscoplastic problem), we understand a process in which the stresses and the strains vary in time and the inertial terms are considered in the movement equations.

The constitutive equation used for finite element analysis of the viscoplastic behavior of the electromagnetically deformed AlMn0.5Mg0.5 material has the expression:

$$\sigma = K \cdot \varepsilon^n \cdot \dot{\varepsilon}^m \tag{9}$$

where σ is the equivalent stress, ε represents the equivalent strain, $\dot{\varepsilon} = d\varepsilon/dt$ is the strain rate.

The same type of constitutive equation was adopted by HU and DAEHN [33] for the simulation of uniaxial tension and the ring expansion with high speed by EMF. Von Mises plasticity criterion was adopted for carrying out the analysis, which has the following formulation in ALGOR software:

$$\sqrt{3 J_2} \geq \sigma_f \tag{10}$$

where

$$J_2 = \frac{1}{6} [(\sigma_1 - \sigma_2)^2 + (\sigma_2 - \sigma_3)^2 + (\sigma_3 - \sigma_1)^2] \tag{11}$$

where σ_f is the flow limit (or $R_{p0.2}$) and σ_1, σ_2 and σ_3 are the principal normal stresses.

This criterion of plasticity was used by UNGER et al [26] for modeling of the EMF process of sheet metal with a circular tool coil. Based on the data files obtained for stresses, subsequently processed with specialized software, the stress distribution was determined in a plan-meridian section and was illustrated in Fig. 5 for points located on the specimen’s surface.

The results referring to stresses were also concretized

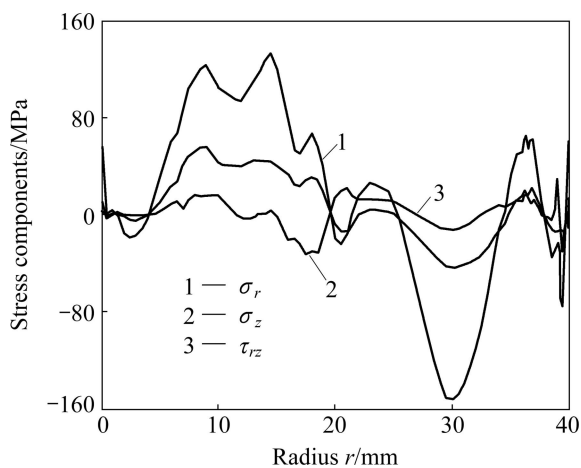


Fig. 5 Stresses variation along radial direction on outer fiber of deformed part

by chromatic representations on color levels, for both the equivalent stress from plastically deformed material and the stress components, for any moment of time during the process. Owing to the fact that the specimen under study is a small thickness disk (0.43 mm), in order to obtain sharp images of the displacement, stress and strain fields, the adopted solution was to divide the plastically deformed part into 20 areas of equal lengths (Fig. 6) and to display them at an increased scale.

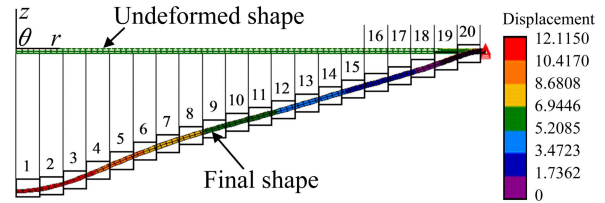


Fig. 6 Sharing (dividing) areas from part

An example regarding the stress field from the formed part is illustrated graphically in Fig. 7.

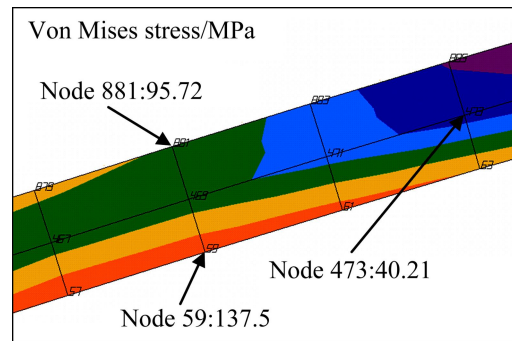


Fig. 7 Field of equivalent stresses from area 8 of modeled part

In the case where Tresca plasticity criterion was used, it was noticed that the equivalent stress determined in the specimen material at the end of the analysis has larger values with about 5.65% as compared to the case where von Mises criterion was used.

The results concerning the displacements could be subjected to comparative analyses due to the use during experiments of some printed disk specimen, having a printed mesh on one side comprising diametrical lines with angular step of 15° and circular lines with radial step of 2 mm (Fig. 8).

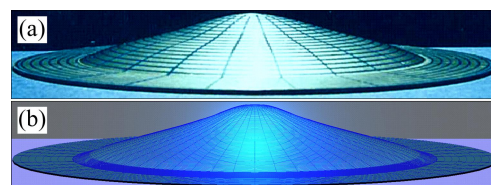


Fig. 8 Photographic image of experimental model (a) and graphic image of finite element model (b)

The validation of the finite element model has been made by comparing the results regarding the axial and radial displacements into common points of both meshes, with those obtained from the experimental data.

The results referring to strains, consisting in numerical values under the form of file data, were subsequently processed with specialized software and the strains distribution in plane-meridian section was obtained, as shown in Fig. 9 for points located on the outer surface of the deformed part.

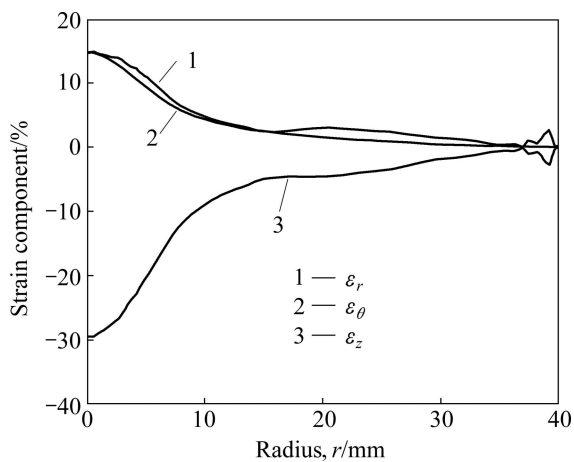


Fig. 9 Strains variation along radial direction on outer fiber of deformed part

Images concerning the field of strains were also obtained for both the equivalent strain and the components of the strain, for any moment of time from the viscoplastic process. For the final moment of the finite element analysis, some results regarding strains from area 4 are presented in Fig. 10.

4 Experiment and measurements for modeling validation

Comparative analyses for stresses are achieved more difficultly in practice. However, accepting the results presented by REPETTO et al [34] for electromagnetic riveting, in which the equivalent stresses of the final analysis with finite elements are shown as residual stresses, a comparative analysis for stresses has been made.

For this purpose, X-ray analysis was performed on a sample cut from the deformed part. The diffraction of the radiations is a means of determining the elastic deformations, from which the real or residual surface stresses can be determined. The residual stresses are caused by the appearance of an asymmetry in the distribution of the strains and the appearance of defects during plastic deformation.

In metals with elementary cell face-centered cube

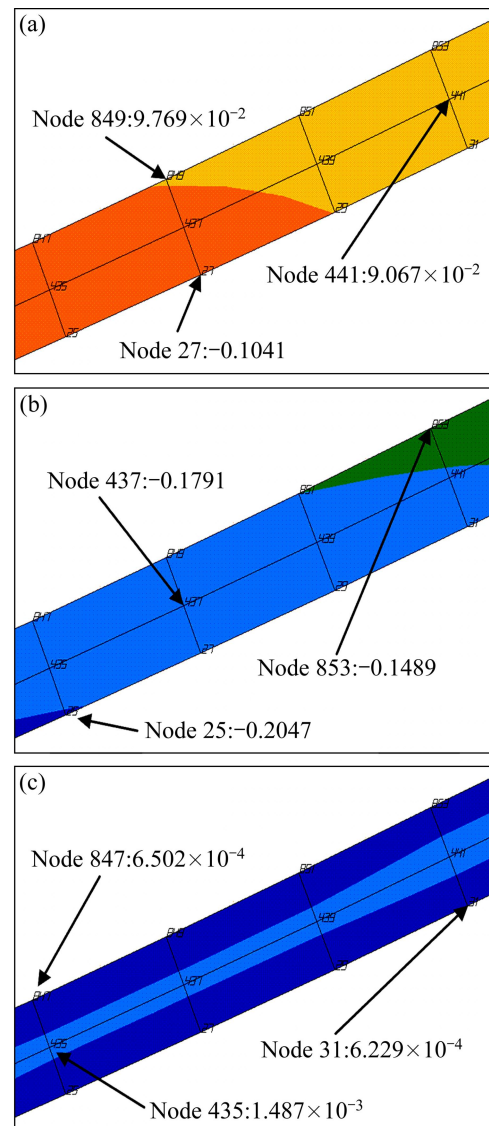


Fig. 10 Field of linear and angular strains from area 4 of modeled specimen: (a) Linear strain, ε_r ; (b) Linear strain, ε_z ; (c) Angular strain, γ_{rz}

type, as that of the model's material, the defects cause asymmetries and displacements of the intensities of diffraction distribution. The stress which causes the deformation can be calculated by determining the interplanar distances d_{0hkl} and d_{hkl} for the unstressed and stressed materials, respectively, and knowing the elastic constants of the material (elastic modulus E and Poisson ratio ν) as well.

The sample, with the approximate dimensions of 16 mm×16 mm, contains the area with radial opening $r=0.385$ mm, and the centre of this square sample positioned at the intersection of the diagonals is considered the correspondent of the radial coordinate $r=(18\pm 0.25)$ mm (node 73, flanked by nodes 72 and 74).

The analysis of the EN AW-3105 alloy was accomplished by means of DRON-2.0 diffractometer, in CAMDRX Laboratory of the National Institute of

Research & Development for Technical Physics of Iasi. For obtaining the diffraction images, radiation Co K α with $\lambda=1.79026 \text{ \AA}$ was used. To perform these analyses with X-ray diffraction, the method presented by GENZEL et al [35] was applied as shown in Fig. 11.

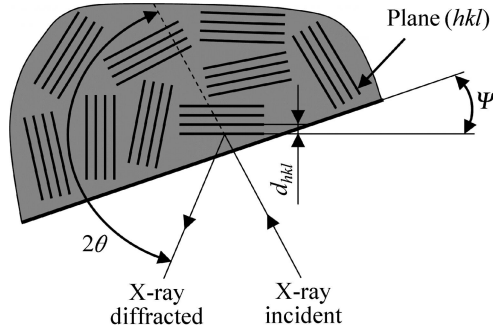


Fig. 11 Working scheme used to analyze stresses by means of X-ray diffraction

Two of the diffractograms obtained for different ψ angles are shown in Fig. 12.

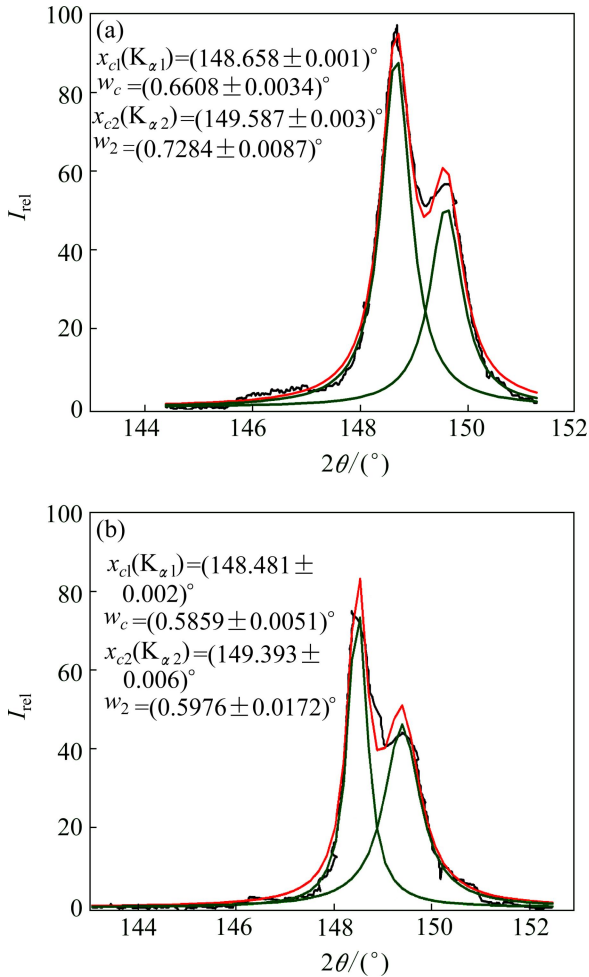


Fig. 12 Diffractograms recorded for extreme values of ψ angle: (a) $\psi=-10^{\circ}$; (b) $\psi=35^{\circ}$

The appearance of two well contoured peaks (maximums) on the diffraction images is due to the real presence of two phases: solid solution $\alpha(\text{Al})$ and $\beta(\text{Al}_6\text{Mn})$ compound. Processing the diffraction images, establishing the integrated intensities of the considered maximums and the calculation of the interplanar distances were accomplished by means of calculating programs initiated and developed by CAMDRX Laboratory. In the above figure, I_{rel} represents the relative intensity of the maximums of diffraction in arbitrary units, x_{c1} and x_{c2} are the positions of the two maximums on the abscissa and w_1 and w_2 are the angular half widths of the two maximum. By processing more diffractograms obtained for different ψ angles, the dependency between relative strain ε_{ψ} and $\sin^2 \psi$ could be determined as [36]

$$\varepsilon_{\psi} = k \sin^2 \psi + \varepsilon_{\perp} \quad (12)$$

where ε_{\perp} is the strain in perpendicular direction and is determined at the intersection of the regression line with the ordinate and k is determined with the following equation:

$$k = \frac{1+\nu}{E} \sigma_{\parallel} = \varepsilon_{\parallel} \quad (13)$$

where ν is the Poisson ratio, E represents the elastic modulus, σ_{\parallel} is the stress in parallel direction at the sample's surface and ε_{\parallel} is the strain in parallel direction.

The relative strain of the material ε_{ψ} was determined by the equation:

$$\varepsilon_{\psi} = (d_{hkl} - d_{0hkl}) / d_{0hkl} \quad (14)$$

The interplanar distances d_{0hkl} and d_{hkl} were determined by Bragg's relation, which has the following form:

$$2d \sin \theta = n_r \lambda \quad (15)$$

where d is the spacing between the planes in the atomic lattice, θ is the diffraction angle, n_r is the reflection order and λ is the wave length of the X radiation.

The data processing and the determination of the regression equation were done by means of specialized software, and the results are shown in Fig. 13.

Based on the relationship between stresses and strains in elastic domain, residual stresses from the specimen could be determined by applying the equations:

$$\sigma_{\perp} = E \varepsilon_{\perp} \equiv \sigma_z \quad (16)$$

$$\sigma_{\parallel} = \frac{E \varepsilon_{\parallel}}{1+\nu} \equiv \sigma_r + \sigma_{\theta} \quad (17)$$

where σ_{\perp} is the stress in perpendicular direction at the sample's surface.

Knowing the elastic constants of the analyzed material ($E=79.827 \text{ GPa}$ and $\nu=0.33$), the residual stresses from the electromagnetically deformed specimen were determined, and the values are indicated in Table 4.

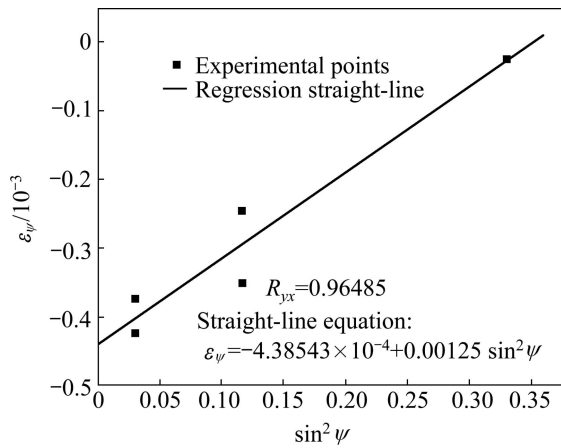


Fig. 13 Determined dependency $\varepsilon_{\psi} - \sin^2 \psi$

Regarding the strains of the electromagnetically deformed part, the comparative analysis between the data established by modeling with finite elements and the data established experimentally was pursued. Table 5 lists a series of results concerning radial strain, noted as ε_r , which offers an image on material’s elongation by EMF.

The initial length of the network element was $l_{e0} = 2$ mm and the radial strain was calculated with the general equation:

$$\varepsilon_r = \frac{l_{e1} - l_{e0}}{l_{e0}} \times 100\% \tag{18}$$

The error between the final length of the element (l_{e1}) of the deformed part resulting from modeling and from the measurement respectively was established with

Table 4 Comparative data concerning stresses

Radius/mm	Reference node	Residual stresses/MPa					
		Established from X-ray analysis		Established from finite element modeling			
		σ_{\perp}	σ_{\parallel}	σ_z	σ_r	σ_{θ}	$\sigma_r + \sigma_{\theta}$
17.75	72	–	–	–32.46	58.56	–6.682	51.878
18	73	–35.004	75.025	–30.82	66.85	–0.761	66.089
18.25	74	–	–	–30.75	57.37	–14.520	42.850

Table 5 Comparative data concerning radial strains

Radius/mm	Node number	Final length of element, l_{e1}			Radial strain, ε_r	
		Determined by modeling/mm	Determined by measuring/mm	Error, e/%	Determined by modeling/%	Determined by measuring/%
0	1	2.26900	2.2300	1.719	13.450	11.50
2	9	2.50987	2.3955	4.557	25.493	19.78
4	17	2.65400	2.4797	6.567	32.700	23.98
6	25	2.69635	2.5157	6.700	34.817	25.78
8	33	2.66833	2.5672	3.790	33.416	28.36
10	41	2.62364	2.7237	–3.814	31.182	36.18
12	49	2.58574	2.5985	–0.494	29.287	29.93
14	57	2.55232	2.5518	0.020	27.616	27.59
16	65	2.52348	2.4891	1.362	26.174	24.46
18	73	2.49658	2.4336	2.522	24.829	21.68
20	81	2.47672	2.4129	2.577	23.836	20.64
22	89	2.45911	2.4419	0.700	22.955	22.09
24	97	2.43787	2.3888	2.013	21.893	19.44
26	105	2.40905	2.3773	1.318	20.452	18.86
28	113	2.37757	2.3303	1.988	18.878	16.51
30	121	2.34856	2.3370	0.492	17.428	16.85
32	129	2.31636	2.3613	–1.940	15.818	18.06
34	137	2.26837	2.3043	–1.584	13.418	15.21
36	145	2.17977	2.2256	–2.103	8.988	11.28
38	169	2.05464	2.0641	–0.461	2.732	3.20
40	201	2.00039	2.0036	–0.160	0.019	0.180

Table 6 Comparative data concerning axial strains

Radius/mm	Node number	Final thickness, t_1			Axial strain, ε_z	
		Determined by modeling/mm	Determined by measuring/mm	Error $e/\%$	Determined by modeling/ $\%$	Determined by measuring/ $\%$
0	1	0.2943	0.310	-5.335	-31.558	-27.91
2	9	0.3024	0.320	-5.820	-29.674	-25.58
4	17	0.3156	0.330	-4.563	-26.605	-23.26
6	25	0.3362	0.340	-1.130	-21.814	-20.93
8	33	0.3604	0.365	-1.276	-16.186	-15.12
10	41	0.3770	0.370	1.857	-12.325	-13.95
12	49	0.3890	0.380	2.314	-9.535	-11.63
14	57	0.3960	0.380	4.040	-7.907	-11.63
16	65	0.4025	0.385	4.348	-6.395	-10.46
18	73	0.4079	0.390	4.388	-5.139	-9.30
20	81	0.4110	0.395	3.893	-4.419	-8.14
22	89	0.4112	0.400	2.724	-4.372	-6.98
24	97	0.4110	0.400	2.676	-4.419	-6.98
26	105	0.4113	0.405	1.532	-4.349	-5.81
28	113	0.4124	0.410	0.582	-4.093	-4.65
30	121	0.4141	0.410	0.990	-3.698	-4.65
32	129	0.4163	0.415	0.312	-3.186	-3.49
34	137	0.4194	0.415	1.049	-2.465	-3.49
36	145	0.4225	0.420	0.592	-1.744	-2.33
38	169	0.4253	0.420	1.246	-1.093	-2.33
40	201	0.4167	0.420	-0.792	-3.093	-2.33

the equation:

$$e = \frac{l_{m1} - l_{m2}}{l_{m1}} \times 100\% \quad (19)$$

where l_{m1} is the value from modeling, l_{m2} is the value from measurement.

Similar data are listed in Table 6 for axial strain deformation $\varepsilon_{z(t)} \equiv \varepsilon_z$, which offers an image on material's thinning of specimen.

The modeling error was found with Eq. (19), the initial thickness of the specimen was $g_0=0.43$ mm and the axial strain (in thickness) was calculated with the equation:

$$\varepsilon_z = \frac{t_1 - t_0}{t_0} \times 100\% \quad (20)$$

5 Conclusions

1) Through finite element modeling, the spring back and residual stresses from the deformed material were obtained.

2) Stress analysis shows a complex stress variation in the deformed material, characterized by an alternation of both tensile and compression stresses with normal and

tangential orientations. This stress variation pattern observed in the electromagnetic deformed part explains the fracture mode of the material in several areas, i.e., in those areas where tensile stresses are acting (located approximately in the radius ranges $r=10-15$ mm and $r=35-40$ mm), that overcome the maximum admissible value.

3) The analysis of the strains obtained by the finite element method shows that the deformed material is subjected to elongations along radial and tangential directions and to thinning along axial direction. Under the circumstances in which the admissible degree of plastic deformation is not exceeded, both elongations and thinning will have maximum values in the centre of the parts and decrease towards the flange area. The used program allows the visualizations of the variation of strains into a meridian plan section for both linear and angular strains.

Acknowledgments

The author thanks to Mr. Mihail-Liviu CRAUS, Ph.D (National Institute of Research & Development for Technical Physics of Iasi), for achieving the diffraction

with X-ray tests and using the software he developed to generate the profile of diffractograms recorded from the figures shown in the paper.

References

- [1] VOHNOUT V J. A quasi-static/dynamic process for forming large sheet metal parts from aluminum alloys [D]. Columbus: The Ohio State University, 1998.
- [2] FENTON G K, DAEHN G S. Modeling of electromagnetically formed sheet metal [J]. *Journal of Materials Processing Technology*, 1998, 75(1–3): 6–16.
- [3] BALANETHIRAM V S, DAEHN G S. Hyperplasticity: Increased forming limits at high workpiece velocity [J]. *Scripta Metallurgica et Materialia*, 1994, 30(4): 515–520.
- [4] ALTYNOVA M, HU X, DAEHN G S. Increased ductility in high velocity electromagnetic ring expansion [J]. *Metallurgical and Materials Transactions A*, 1996, 27A: 1837–1844.
- [5] VOHNOUT V J, DAEHN G, SHIVPURI R. A hybrid quasi-static-dynamic process for increased limiting strains in the forming of large sheet metal aluminum parts [C]// *Proceedings of the 6th International Conference on Technology of Plasticity*. Nurnberg, Germany, 1999: 1359–1364.
- [6] PADMANABHAN M. Wrinkling and springback in electromagnetic sheet metal forming and electromagnetic ring compression [D]. Columbus: The Ohio State University, 1997.
- [7] DAEHN G S. High velocity metal forming [M]// *ASM Handbook, Volume 14B: Metalworking: Sheet forming*. Ohio: ASM International, 2006: 405–418.
- [8] BALANETHIRAM V S, HU X, ALTYNOVA M, DAEHN G S. Hyperplasticity: Enhanced formability at high rates [J]. *Journal of Materials Processing Technology*, 1994, 45(1–4): 595–600.
- [9] DAEHN G S, ALTYNOVA M, BALANETHIRAM V S, FENTON G, PADMANABHAN M, TAMHANE A A, WINNARD E. High velocity metal forming—an old technology addresses new problems [J]. *JOM*, 1995, 47(7): 42–45.
- [10] ERNST R, GILLON P, MALLEIN V, GARNIER M. Finite element modeling of electromagnetic sheet metal forming [C]// *Proceedings of the 4th International Conference on Electromagnetic Processing of Materials*. Lyon, France, 2003: 301–306.
- [11] PARK Y B, KIM H Y, OH S I. Design of axial/torque joint made by electromagnetic forming [J]. *Thin-Walled Structures*, 2005, 43(5): 826–844.
- [12] RISCH D, GERSTEYN G, DUDZINSKI W, BEERWALD C, BROSIUS A, SCHAPER M, TEKKAYA A E, BACH F W. Design and analysis of a deep drawing and in-process electromagnetic sheet metal forming process [C]// *Proceedings of the 3rd International Conference on High Speed Forming*. Dortmund, Germany, 2008: 201–212.
- [13] TAKATSU N, KATO M, SATO K, TOBE T. High-speed forming of metal sheets by electromagnetic force [J]. *Japan Society of Mechanical Engineers, International Journal Part C*, 1988, 31(1): 142–148.
- [14] CORREIA J P M, SIDDIQUI M A, AHZI S, BELOUETTAR S, DAVIES R. A simple model to simulate electromagnetic sheet free bulging process [J]. *International Journal of Mechanical Sciences*, 2008, 50(10–11): 1466–1475.
- [15] AHMED M, PANTHI S K, RAMAKRISHNAN N, JHA A K, YEGNESWARAN A H, DASGUPTA R, AHMED S. Alternative flat coil design for electromagnetic forming using FEM [J]. *Transactions of Nonferrous Metals Society of China*, 2011, 21(3): 618–625.
- [16] CUI Xiao-hua, MO Jian-hua, XIAO Shu-jie, DU Er-hu. Magnetic force distribution and deformation law of sheet using uniform pressure electromagnetic actuator [J]. *Transactions of Nonferrous Metals Society of China*, 2011, 21(11): 2484–2489.
- [17] LI C, ZHAO Z, LI J, WANG Y, YANG Y. Numerical simulation of the magnetic pressure in tube electromagnetic bulging [J]. *Journal of Materials Processing Technology*, 2002, 123: 225–228.
- [18] KARCH C, ROLL K. Transient simulation of electromagnetic forming of aluminium tubes [J]. *Advanced Materials Research*, 2005, 6–8: 639–648.
- [19] CAO Q, LI L, LAI Z, ZHOU Z, XIONG Q, ZHANG X, HAN X. Dynamic analysis of electromagnetic sheet metal forming process using finite element method [J]. *International Journal of Advanced Manufacturing Technology*, 2014, 74: 361–368.
- [20] SIDDIQUI M A, CORREIA J P M, AHZI S, BELOUETTAR S. A numerical model to simulate electromagnetic sheet metal forming [J]. *International Journal of Material Forming*, 2008, 1(Suppl 1): 1387–1390.
- [21] SIDDIQUI M A, CORREIA J P M, AHZI S, BELOUETTAR S. Electromagnetic forming process: Estimation of magnetic pressure in tube expansion and numerical simulation [J]. *International Journal of Material Forming*, 2009, 2(Suppl 1): 649–652.
- [22] CUI X, MO J, XIAO S, DU E, ZHAO J. Numerical simulation of electromagnetic sheet bulging based on FEM [J]. *International Journal of Advanced Manufacturing Technology*, 2011, 57: 127–134.
- [23] LIU Da-hai, LI Cun-feng, YU Hai-ping. Numerical modeling and deformation analysis for electromagnetically assisted deep drawing of AA5052 sheet [J]. *Transactions of Nonferrous Metals Society of China*, 2009, 19(5): 1294–1302.
- [24] LUCA D. A numerical modelling: Opened perspectives to increase the performance of the electromagnetic forming processes [J]. *International Journal of Numerical Modelling: Electronic Networks, Devices and Fields*, 2012, 25: 15–23.
- [25] XU Wei, FANG Hong-yuan, CAO Jun, DING Wen-bin, SHAN Ping. Parametric effect of large impulse current excited coil on electromagnetic force in coil-sheet system [J]. *Transactions of Nonferrous Metals Society of China*, 2009, 19(S3): S806–S810.
- [26] UNGER J, STIEMER M, SVENDSEN B, BLUM H. Multifield modeling of electromagnetic metal forming processes [J]. *Journal of Materials Processing Technology*, 2006, 177: 270–273.
- [27] BAHMANI M A, NIAYESH K, KARIMI A. 3D simulation of magnetic field distribution in electromagnetic forming systems with field-shaper [J]. *Journal of Materials Processing Technology*, 2009, 209: 2295–2301.
- [28] UNGER J, STIEMER M, SCHWARZE M, SVENDSEN B, BLUM H, REESE S. Modelling and simulation of 3D electromagnetic metal forming processes [J]. *International Journal of Material Forming*, 2008, 1(Suppl 1): 1399–1402.
- [29] CUI X H, MO J H, ZHU Y. 3D modeling and deformation analysis for electromagnetic sheet forming process [J]. *Transactions of Nonferrous Metals Society of China*, 2012, 22(1): 164–169.
- [30] Technical specification: alloy 3105. [EB/OL][2014–05–08]. [Http://www.emiratesrecycling.com/sites/emiratesrecycling.com/themes/emr/images/TechnicalSpecification.pdf](http://www.emiratesrecycling.com/sites/emiratesrecycling.com/themes/emr/images/TechnicalSpecification.pdf).
- [31] SAFARI M, HOSSEINIPOUR S J, AZODI H D. An investigation into the effect of strain rate on forming limit diagram using ductile fracture criteria [J]. *Meccanica*, 2012, 47(6): 1391–1399.
- [32] CRISTESCU N D. *Dynamic plasticity* [M]. Singapore: World Scientific Publishing Company, 2007.
- [33] HU X, DAEHN G S. Effect of velocity on flow localization in

- tension [J]. *Acta Materialia*, 1996, 44(3): 1021–1033.
- [34] REPETTO E A, RADOVIITZKY R, ORTIZ M. A finite element study of electromagnetic riveting [J]. *Journal of Manufacturing Science and Engineering*, 1999, 121: 61–68.
- [35] GENZEL C, BRODA M, DANTZ D, REIMERS W. A self-consistent method for X-ray diffraction analysis of multiaxial residual-stress fields in the near-surface region of polycrystalline materials. I. Theoretical concept [J]. *Journal of Applied Crystallography*, 1999, 32(4): 770–778.
- [36] GENZEL C, BRODA M, DANTZ D, REIMERS W. A self-consistent method for X-ray diffraction analysis of multiaxial residual-stress fields in the near-surface region of polycrystalline materials. II. Examples [J]. *Journal of Applied Crystallography*, 1999, 32(4): 779–787.

AlMg0.5Mg0.5 板材电磁成形过程的有限元模拟与试验研究

Dorin LUCA

Department of Technologies and Equipments for Materials Processing,
Technical University of Iasi, 700050 Iasi, Romania

摘要: 电磁成形是一种高速成形技术, 可以提高一些塑性变形金属的成形性。为评价轻金属如铝和铝合金的电磁成形的能力, 需要研究材料成形过程中的应力和应变状态。对电磁成形 AlMn0.5Mg0.5 板材的应力和应变进行有限元建模并通过实验进行验证。采用 X 射线衍射确定材料中的残余应力。采用三轴试验机, 通过刻在样品上网格点的位移计算应变。建模结果与实验数据具有很好的一致性。

关键词: 有限元模拟; 电磁成形; AlMn0.5Mg0.5 板材; X 射线衍射; 应力; 应变

(Edited by Yun-bin HE)